

# First constraints on QCD axion dark matter using James Webb Space Telescope observations

Elena Pinetti<sup>1,2,3,4,\*</sup>

<sup>1</sup>*Center for Computational Astrophysics, Flatiron Institute, New York, NY 10010, USA*

<sup>2</sup>*Emmy Noether Fellow, Perimeter Institute for Theoretical Physics,  
31 Caroline Street N., Waterloo, Ontario, N2L 2Y5, Canada*

<sup>3</sup>*Theoretical Physics Division, Fermi National Accelerator Laboratory, Batavia, IL, USA*

<sup>4</sup>*Kavli Institute for Cosmological Physics, University of Chicago, Chicago, IL USA*

I present the first constraints on QCD axion dark matter using measurements from the James Webb Space Telescope. By utilizing publicly available MIRI and NIRSpec blank-sky observations, originally collected for sky subtraction purposes, I derive strong limits on the axion-photon coupling constant  $g_{a\gamma\gamma}$  in the mass range 0.1–4 eV. These constraints improve upon previous studies by more than two orders of magnitude for a range of masses. This analysis underscores the potential of blank-sky observations as a powerful tool for constraining dark matter models and demonstrates how astrophysical missions can be repurposed for particle physics research.

## I. INTRODUCTION

Unraveling the nature of dark matter (DM) is a fundamental challenge in modern physics. Although cosmological and astrophysical observations strongly support the existence of DM, its microscopic properties remain elusive (see Ref. [1] for a review). Plausible beyond-the-Standard Model (BSM) theories suggest that DM could be unstable and decay into Standard Model particles on a cosmological timescale [2–4]. Among the BSM models proposing viable DM candidates, the axion stands out as one of the most promising options (see Ref. [5] for a review). Initially introduced to resolve the strong charge-parity (CP) problem in quantum chromodynamics (QCD) [6–9], these pseudoscalar particles can interact with Standard Model particles and decay into two photons. The theory of QCD axions has inspired various extensions of the Standard Model, proposing pseudoscalar DM candidates that possess similar coupling to photons but do not resolve the strong CP problem. These particles are referred to as axion-like particles (ALPs) [10]. Due to energy conservation, eV-scale axions are expected to decay into infrared and optical photons. Space- and ground-based telescopes provide a promising means to detect such decay signals (e.g. Refs. [11, 12]). Previous studies in this mass range have primarily focused on targeted observations of dwarf galaxies, globular clusters, and galaxy clusters [13–21].

The advent of the James Webb Space Telescope has provided a new avenue to constrain DM scenarios using blank-sky observations [11]. These fields represent a significant untapped resource for DM studies due to the huge amount of data accessible. This is because blank-sky observations are routinely conducted for background subtraction in most astronomical surveys, meaning it is possible to use nearly the entire area surveyed by JWST instead of only the area around a few specific targets.

Furthermore, the data are publicly available, allowing axion searches to be performed without requiring additional dedicated telescope time.

In this paper, I present the first constraints from JWST observations on QCD axion dark matter down to masses of 0.1 eV.<sup>1</sup> This is the first time data from the JWST Mid-Infrared Instrument (MIRI) spectrograph have been used for this purpose. MIRI’s wavelength coverage of 4.9–28.5  $\mu\text{m}$  enables the exploration of the QCD axion parameter space at lower masses than any previous ground- or space-based telescopes. Besides using over 15,000 MIRI measurements, I perform a multi-target analysis using over 3,600 NIRSpec observations, which extends the mass range to 0.5–4 eV. Throughout this work, I adopt natural units where  $\hbar = c = 1$ , unless stated otherwise.

## II. AXION SIGNAL

I searched for infrared emission lines originating from axion decays into two photons, within the Milky Way halo. The axion-photon interaction is described by a term in the Lagrangian

$$\mathcal{L}_a = -\frac{1}{4}g_{a\gamma\gamma}aF_{\mu\nu}\tilde{F}^{\mu\nu}, \quad (1)$$

where  $a$  denotes the axion field,  $F_{\mu\nu}$  represents the electromagnetic field strength tensor and  $\tilde{F}_{\mu\nu}$  is its dual. The strength of the axion-photon interaction is characterized by the axion-photon coupling  $g_{a\gamma\gamma}$ . The expected observed flux for such an emission can be expressed as

$$\phi_a = \frac{1}{4\pi} \frac{g_{a\gamma\gamma}^2 m_a^3}{64\pi} \left( \frac{df}{d\nu} * \mathcal{W} \right) \mathcal{D}, \quad (2)$$

<sup>1</sup> At the masses of interest here, some QCD axion models are constrained by observations of supernovae [22] and neutron stars [23] but these bounds are evaded by flavor non-universal scenarios [24–26], permitting the existence of QCD axions with masses  $\text{meV} \lesssim m_a \lesssim \text{eV}$  [27–30].

\* [epinetti@flatironinstitute.org](mailto:epinetti@flatironinstitute.org)

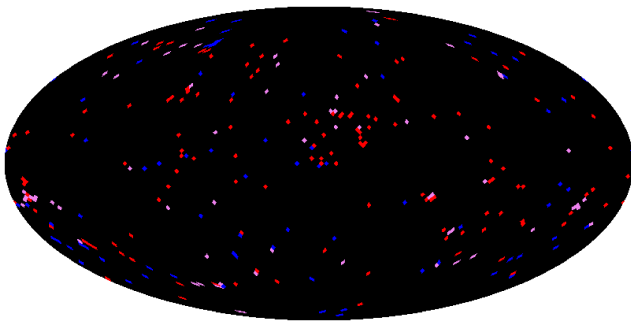


FIG. 1. Map of the targets used in this analysis: targets observed both with NIRSpec and MIRI (purple dots), targets observed only with NIRSpec (blue), only with MIRI (red).

where  $m_a$  is the axion mass. The D-factor  $\mathcal{D}(\theta) = \int ds \rho$  is the DM column density for a given DM space density  $\rho$ , over the line-of-sight distance  $s$ . The DM density profile is assumed to be a standard NFW profile with  $r_s = 24$  kpc and  $\rho_s = 0.18$  GeV/cm<sup>3</sup> [31–33], and in Section V I discuss the uncertainty associated with a different choice of the DM profile. The emission spectrum  $df/d\nu$  describes the fraction of total luminosity emitted in the frequency range  $d\nu$ . The shape of the spectrum is largely determined by Doppler broadening and therefore depends on the DM velocity distribution. I model the DM velocity distribution as a uniform, isotropic Maxwell–Boltzmann distribution with dispersion  $\sigma_v = 160$  km/s [34]. The emission spectrum  $df/d\lambda$  is then a normal distribution with standard deviation  $\sigma_0 = \lambda_0 \sigma_v$  and  $\lambda_0 = 4\pi/m_a$ . The observed flux is given by the convolution of the emission spectrum with the instrumental response function  $\mathcal{W}$ , which I model as a Gaussian distribution in wavelength [11, 35, 36]. The relation between the dispersion  $\sigma_\lambda$  and the instrumental full width at half maximum  $\Delta\lambda$  is given by  $\sigma_\lambda = \Delta\lambda/2\sqrt{2}$ . Hence, the observed line emission is modeled as a Gaussian distribution with variance  $\sigma^2 = \sigma_\lambda^2 + \sigma_0^2$ .

### III. JAMES WEBB SPACE TELESCOPE BLANK-SKY OBSERVATIONS

The James Webb Space Telescope (JWST) [37] is an infrared observatory with instruments spanning the wavelength range (0.6–28.3  $\mu\text{m}$ ). In this analysis, I employ observations from two spectrographs on JWST, namely the Near-Infrared Spectrograph (NIRSpec, 0.6–5  $\mu\text{m}$ ) and the Mid-Infrared Instrument (MIRI, 4.9–28.5  $\mu\text{m}$ ). Both instruments provide integral field unit (IFU) spectrographs well-suited for blank-sky axion searches. NIRSpec covers 0.6  $\mu\text{m}$  to 5.3  $\mu\text{m}$  across a 3"  $\times$  3" field of view and includes high-resolution gratings ( $R \sim 2700$ ), three medium-resolution gratings ( $R \sim 1000$ ), one low-resolution prism ( $R \sim 100$ ) [38, 39]. MIRI provides spectral resolution  $R \sim 1500$ –3500 over the wavelength range

4.9 to 28.8  $\mu\text{m}$  and a 3.5"  $\times$  3.5" field of view [40–42]. The observations used in this analysis include 138 targets for a total observation time of 1064 hours with NIRSpec, and 282 targets observed for 3770 hours with MIRI. The sky coordinates of these observations are shown in Fig. 1: the red dots refer to MIRI targets, the blue dots are NIRSpec targets and the purple dots denote the targets that both instruments have observed. Table I and Table II report 10 example targets for NIRSpec and MIRI, respectively. Note that I utilized blank-sky observations taken as calibration sky flats for these target observations. For each blank-sky target in the table, the total observation time, D-factor  $\mathcal{D}$ , and observed wavelength range are listed. All the MIRI and NIRSpec data used in this paper were downloaded from the MAST database [43]. The specific observations analyzed can be accessed via <https://github.com/elenapinetti/JWST-data>.

### IV. DATA ANALYSIS

I search for an axion signal, setting bounds on the axion-photon coupling  $g_{a\gamma\gamma}$  as a function of the axion mass  $m_a$ . The observed emission is modeled as the sum of two contributions:

$$\mathcal{E}(\lambda|g_{a\gamma\gamma}, \theta) = \phi_a(\lambda, g_{a\gamma\gamma}) + \mathcal{B}(\lambda, \theta), \quad (3)$$

where  $\phi_a$  represents an axion component, given by Eq. (2), and  $\mathcal{B}$  is a background term, parameterized in terms of nuisance parameters  $\theta$ . The blank-sky fields used in this analysis are off-target observations, therefore they are expected to be dominated by background emission. Indeed, the entire purpose of these blank-sky observations is to measure and subtract the local background emission from target observations. The goal of this work however is to find an axion line hidden in this overwhelming background. It is therefore crucial to remove as much astrophysical background as possible to maximize the sensitivity to axion lines.

The astrophysical background has four main components: zodiacal light, detector thermal self-emission, stray light, and interstellar medium (ISM) background associated with the dust emission within the Milky Way. Unfortunately, there is not a sufficiently accurate parametric description of these backgrounds. The JWST backgrounds tool [44] provides a rough estimate of these background emission components. However, a cursory comparison between the JWST tool predictions for these backgrounds and the actual measurements demonstrates that the tool does not provide a sufficiently accurate prediction to remove the backgrounds well enough to detect underlying axion emissions.

A more general approach to estimating the background is therefore necessary. Rather than assuming a parametric model for the background emission, I adopt a flexible approach, in which the spectrum of the total background is treated as a smooth polynomial *locally* in wavelength,

Target name	Observation time [hr]	$\Delta\lambda$ [ $\mu\text{m}$ ]	D-factor [ $10^{22} \text{ GeV}/\text{cm}^2$ ]
GC	58.4	1.66-3.17	17.9
B335	4.020	2.87-5.27	2.35
IRAS 16253-2429	3.9	2.87-5.27	4.46
IRAS 20126+4104	6.808	2.87-5.27	1.45
HOPS370	3.112	2.87-5.27	0.876
LQAC 308-047 001	7.846	0.97-1.89	2.74
HE 0435-1223	15.691	0.97-1.89	0.913
HOPS153	6.030	2.87-5.27	0.882
RXCJ0600-z6	12.7	2.87-5.27	0.935
C/2014 UN271	10.5	0.60-5.30	1.30

TABLE I. Examples of some of the most constraining blank-sky NIRSpec observations. For each blank-sky target in the table, the total observation time (second column), observed wavelength range (third column), and D-factor  $\mathcal{D}$  (fourth column) are listed.

Target name	Observation time [hr]	$\lambda$ [ $\mu\text{m}$ ]	D-factor [ $10^{22} \text{ GeV}/\text{cm}^2$ ]
IRAC J123711.88+622212.5	12.741	5.66-24.48	1.07
SDSSJ1652+1728	30.791	4.90-20.95	2.23
M-83-F1	75.5	4.90-28.6	2.04
XID2028	35.410	4.90-20.95	1.04
SPT0346-52	29.0	4.90-24.5	1.21
C/2017 K2	48.8	4.90-28.6	3.58
SPT-S J031134-5823.5	60.7	4.90-24.5	1.31
IRAS 01364-1042	53.513	4.90-28.70	1.08
SGAS J122651.3+215220	15.1	6.53-28.6	1.25
2MASS J04202144+2813491	54.947	4.90-28.70	0.840

TABLE II. Same as in Table I but for MIRI.

as described in detail in Appendix A. The width of the region used for the polynomial fit is discussed in Appendix B, while the uncertainty associated with this model is addressed in Appendix C. To prevent the analysis from being affected by possible astrophysical absorption lines, I exclude observations where an absorption line is detected, as explained in Appendix D.

Following Refs. [33, 45, 46], I define the goodness of fit  $\chi^2$ :

$$\chi^2(g_{a\gamma\gamma}, \boldsymbol{\theta}) = \sum_{i,j} \left( \frac{\mathcal{E}(\lambda_{i,j}|g_{a\gamma\gamma}, \boldsymbol{\theta}_i) - d_{i,j}}{\sigma_{i,j}} \right)^2, \quad (4)$$

where  $\boldsymbol{\theta}$  are the nuisance parameters of the smooth background, and  $d_i$  represents the JWST observations. The index  $i$  runs over the dataset, while the index  $j$  runs over the wavelength. I can derive a profile likelihood for  $g_{a\gamma\gamma}$  by optimizing over  $\boldsymbol{\theta}$ . Specifically, let us define the  $\chi^2(g_{a\gamma\gamma}) \equiv \chi^2(g_{a\gamma\gamma}, \hat{\boldsymbol{\theta}})$ , where  $\hat{\boldsymbol{\theta}}$  minimizes the  $\chi^2$  of Eq. (4) at fixed  $g_{a\gamma\gamma}$ . I derive the constraints on the axion-photon coupling  $g_{a\gamma\gamma}$  using the  $\chi^2(g_{a\gamma\gamma})$  defined above, by scanning over  $g_{a\gamma\gamma}$ . The maximum likelihood estimate of  $g_{a\gamma\gamma}$  is the value that minimizes  $\chi^2(g_{a\gamma\gamma})$  and the 95% confidence region corresponds to the range of  $g_{a\gamma\gamma}$  where  $\Delta\chi^2 \leq 3.84$  relative to the global minimum.

## V. RESULTS

The 95% constraints on the axion-photon coupling  $g_{a\gamma\gamma}$  as a function of the axion mass  $m_a$  are shown in Fig. 2. These bounds assume that axions constitute the entire dark matter content of the Milky Way halo. The red line refers to the limits derived using 15,419 blank-sky observations of MIRI, while in blue I show the bounds obtained with 3,639 sky flat measurements taken by NIRSpec. MIRI data constrains the mass range 0.1-0.5 eV, while NIRSpec limits higher masses between 0.5 and 4 eV. The yellow band corresponds to the QCD axion band, i.e. the region of the parameter space where axions could simultaneously comprise the dark matter and solve the strong CP problem of quantum chromodynamics. The grey area is already constrained by indirect searches for axion decay with MUSE [14], WINERED [16], and helioscope searches for axion-like particles by CAST [47, 48]. Refs. [20, 21] argue that the region above the dotted line is disfavored based on the impact of axion emission on stellar evolution. However, there is considerable complexity in setting such limits as shown in Ref. [49]. Existing limits are drawn from Refs. [50, 51].

The results derived in this analysis have two important implications: 1) they represent the first constraints on QCD axion dark matter using JWST observations and,

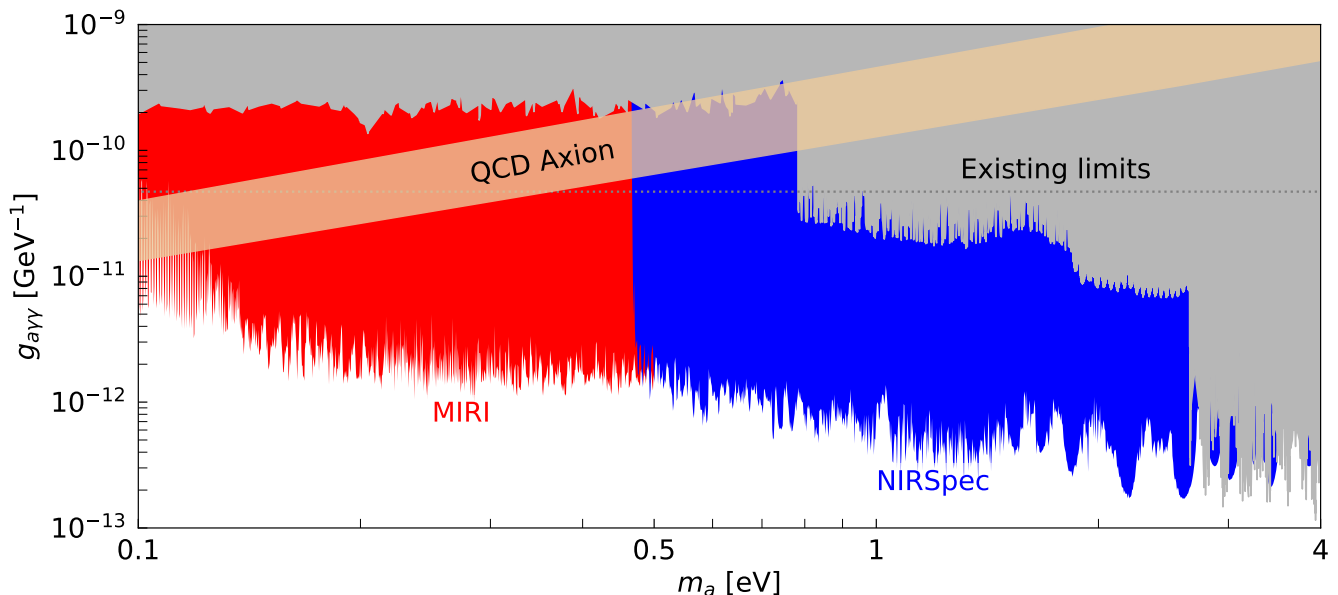


FIG. 2. New constraints on QCD axion dark matter and axion-like particles using MIRI (red) and NIRSpec (blue) blank-sky observations. The yellow band represents the parameter values where the QCD axion can comprise all the dark matter. Existing limits are discussed in the text.

more generally, infrared telescopes down to masses of 0.1 eV; 2) they significantly improve over existing bounds, in some cases by more than two orders of magnitude. At certain wavelengths, features consistent with lines are found with high significance. Many of these lines are consistent with known atomic and molecular lines. I leave to future work to explore their origin, and potentially mitigate their effect to allow for even stronger constraints to be derived.

Note that the bounds derived in this analysis using JWST data are stronger than the projections in Ref. [11]. This improvement is due to the fact that the authors focused on two NIRSpec observations of the GN-z11 sky flats with an observing time of less than an hour. They then estimated the telescope’s reach by conservatively scaling their results based on an integration time equal to 3% of the total JWST mission lifetime, assumed to be 15 years. These projections, however, neglect the important effects of using blank-sky observations in regions with a larger expected axion signal, such as the Galactic Center. Furthermore, NIRSpec has already accumulated over 1064 hours of observation, and MIRI over 3770 hours, which means that their sensitivity reach to dark matter signals by the end of the mission is even greater than previously expected.

## VI. CONCLUSION

This study constrains QCD axion dark matter for the first time using measurements from the James Webb Space Telescope (JWST), down to masses of 0.1 eV. I use publicly available blank-sky observations, originally

gathered for sky subtraction purposes with the MIRI and NIRSpec spectrographs.

This blank-sky strategy enables future axion searches to be consistently updated and enhanced as JWST operations progress, since every observation will provide sky flats, regardless of the specific targets chosen for upcoming observations. This analysis demonstrates that blank-sky observations with infrared telescopes are a powerful tool for constraining dark matter models and for repurposing astrophysical missions for particle physics.

## ACKNOWLEDGMENTS

I thank Ryan Janish for help in obtaining the data used in this project. I thank Aurelio Amerio, Duncan Adams, Nikita Blinov, Neal Dalal, Chris Dessert, David Dunsky, Junwu Huang, Gordan Krnjaic, Mariangela Lisanti, Karin Sandstrom, Oren Slone and Ken Van Tilburg for helpful conversations.

EP is grateful for the hospitality of Perimeter Institute where part of this work was carried out. Research at Perimeter Institute is supported in part by the Government of Canada through the Department of Innovation, Science and Economic Development and by the Province of Ontario through the Ministry of Colleges and Universities. The data presented in this paper were obtained from the Mikulski Archive for Space Telescopes (MAST) at the Space Telescope Science Institute (STScI). STScI is operated by the Association of Universities for Research in Astronomy, Inc., under NASA contract NAS5-26555. Support to MAST for these data is provided by the NASA Office of Space Science via grant NAG5-7584 and



by other grants and contracts. I acknowledge support from *Fermi Research Alliance, LLC* under Contract No.

DE-AC02-07CH11359 with the U.S. Department of Energy, Office of High Energy Physics.

- 
- [1] M. Cirelli, A. Strumia and J. Zupan, *Dark Matter*, **2406.01705**.
- [2] T.R. Slatyer, *Indirect detection of dark matter.*, in *Theoretical Advanced Study Institute in Elementary Particle Physics: Anticipating the Next Discoveries in Particle Physics*, pp. 297–353, 2018, DOI [1710.05137].
- [3] D. Hooper, *TASI Lectures on Indirect Searches For Dark Matter*, *PoS TASI2018* (2019) 010 [1812.02029].
- [4] B.R. Safdi, *TASI Lectures on the Particle Physics and Astrophysics of Dark Matter*, *PoS TASI2022* (2024) 009 [2303.02169].
- [5] C.A.J. O’Hare, *Cosmology of axion dark matter*, *PoS COSMICWISPERs* (2024) 040 [2403.17697].
- [6] R.D. Peccei and H.R. Quinn, *Constraints imposed by CP conservation in the presence of pseudoparticles*, *Phys. Rev. D* **16** (1977) 1791.
- [7] R.D. Peccei and H.R. Quinn, *CP conservation in the presence of pseudoparticles*, *Phys. Rev. Lett.* **38** (1977) 1440.
- [8] F. Wilczek, *Problem of strong p and t invariance in the presence of instantons*, *Phys. Rev. Lett.* **40** (1978) 279.
- [9] S. Weinberg, *The u(1) problem*, *Phys. Rev. D* **11** (1975) 3583.
- [10] C.B. Adams et al., *Axion Dark Matter*, in *Snowmass 2021*, 3, 2022 [2203.14923].
- [11] R. Janish and E. Pinetti, *Hunting Dark Matter Lines in the Infrared Background with the James Webb Space Telescope*, **2310.15395**.
- [12] S. Roy, C. Blanco, C. Dessert, A. Prabhu and T. Temim, *Sensitivity of JWST to eV-Scale Decaying Axion Dark Matter*, **2311.04987**.
- [13] M. Regis, M. Taoso, D. Vaz, J. Brinchmann, S.L. Zoutendijk, N.F. Bouché et al., *Searching for light in the darkness: Bounds on ALP dark matter with the optical MUSE-faint survey*, *Phys. Lett. B* **814** (2021) 136075 [2009.01310].
- [14] E. Todarello, M. Regis, J. Reynoso-Cordova, M. Taoso, D. Vaz, J. Brinchmann et al., *Robust bounds on ALP dark matter from dwarf spheroidal galaxies in the optical MUSE-Faint survey*, **2307.07403**.
- [15] D. Grin, G. Covone, J.-P. Kneib, M. Kamionkowski, A. Blain and E. Jullo, *A Telescope Search for Decaying Relic Axions*, *Phys. Rev. D* **75** (2007) 105018 [astro-ph/0611502].
- [16] W. Yin et al., *First Result for Dark Matter Search by WINERED*, *Phys. Rev. Lett.* **134** (2025) 051004 [2402.07976].
- [17] A. Caputo, A. Vittino, N. Fornengo, M. Regis and M. Taoso, *Searching for axion-like particle decay in the near-infrared background: an updated analysis*, *JCAP* **05** (2021) 046 [2012.09179].
- [18] P. Carenza, G. Lucente and E. Vitagliano, *Probing the blue axion with cosmic optical background anisotropies*, *Phys. Rev. D* **107** (2023) 083032 [2301.06560].
- [19] K. Nakayama and W. Yin, *Anisotropic cosmic optical background bound for decaying dark matter in light of the LORRI anomaly*, *Phys. Rev. D* **106** (2022) 103505 [2205.01079].
- [20] A. Ayala, I. Domínguez, M. Giannotti, A. Mirizzi and O. Straniero, *Revisiting the bound on axion-photon coupling from Globular Clusters*, *Phys. Rev. Lett.* **113** (2014) 191302 [1406.6053].
- [21] M.J. Dolan, F.J. Hiskens and R.R. Volkas, *Advancing globular cluster constraints on the axion-photon coupling*, *JCAP* **10** (2022) 096 [2207.03102].
- [22] A. Lella, P. Carenza, G. Co’, G. Lucente, M. Giannotti, A. Mirizzi et al., *Getting the most on supernova axions*, *Physical Review D* **109** (2024) .
- [23] M. Buschmann, C. Dessert, J.W. Foster, A.J. Long and B.R. Safdi, *Upper limit on the qcd axion mass from isolated neutron star cooling*, *Physical Review Letters* **128** (2022) .
- [24] L. Di Luzio, F. Mescia, E. Nardi, P. Panci and R. Ziegler, *Astrophobic axions*, *Physical Review Letters* **120** (2018) .
- [25] F. Björkeröth, L. Di Luzio, F. Mescia and E. Nardi, *U(1) flavour symmetries as peccei-quinn symmetries*, *Journal of High Energy Physics* **2019** (2019) .
- [26] M. Badziak and K. Harigaya, *Naturally astrophobic qcd axion*, *Journal of High Energy Physics* **2023** (2023) .
- [27] R.T. Co, L.J. Hall and K. Harigaya, *Qcd axion dark matter with a small decay constant*, *Physical Review Letters* **120** (2018) .
- [28] A. Caputo and M. Reig, *Cosmic implications of a low-scale solution to the axion domain wall problem*, *Physical Review D* **100** (2019) .
- [29] L. Visinelli and P. Gondolo, *Axion cold dark matter in nonstandard cosmologies*, *Physical Review D* **81** (2010) .
- [30] R.T. Co, L.J. Hall and K. Harigaya, *Axion kinetic misalignment mechanism*, *Physical Review Letters* **124** (2020) .
- [31] J.F. Navarro, C.S. Frenk and S.D.M. White, *The Structure of cold dark matter halos*, *Astrophys. J.* **462** (1996) 563 [astro-ph/9508025].
- [32] M. Cirelli, G. Corcella, A. Hektor, G. Hutsi, M. Kadastik, P. Panci et al., *PPPC 4 DM ID: A Poor Particle Physicist Cookbook for Dark Matter Indirect Detection*, *JCAP* **03** (2011) 051 [1012.4515].
- [33] M. Cirelli, N. Fornengo, B.J. Kavanagh and E. Pinetti, *Integral X-ray constraints on sub-GeV Dark Matter*, *Phys. Rev. D* **103** (2021) 063022 [2007.11493].
- [34] N.W. Evans, C.A.J. O’Hare and C. McCabe, *Refinement of the standard halo model for dark matter searches in light of the Gaia Sausage*, *Phys. Rev. D* **99** (2019) 023012 [1810.11468].
- [35] P. Jakobsen, P. Ferruit, C. Alves de Oliveira, S. Arribas, G. Bagnasco, R. Barho et al., *The Near-Infrared Spectrograph (NIRSpec) on the James Webb Space Telescope. I. Overview of the instrument and its capabilities*, *Astron. Astrophys.* **661** (2022) A80 [2202.03305].
- [36] “Nirspec dispersers and filters.” <https://jwst-docs.stsci.edu/jwst-near-infrared-spectrograph/nirspec-instrumentation/>

- nirspec-dispersers-and-filters, 2017.
- [37] J.P. Gardner et al., *The James Webb Space Telescope, Space Sci. Rev.* **123** (2006) 485 [astro-ph/0606175].
- [38] <https://jwst-docs.stsci.edu/jwst-near-infrared-spectrograph#gsc.tab=0>.
- [39] <https://jwst-docs.stsci.edu/jwst-near-infrared-spectrograph/nirspec-instrumentation/nirspec-dispersers-and-filters#gsc.tab=0>.
- [40] G.H. Rieke, G.S. Wright, T. Böker, J. Bouwman, L. Colina, A. Glasse et al., *The Mid-Infrared Instrument for the James Webb Space Telescope, I: Introduction, Publications of the Astronomical Society of the Pacific* **127** (2015) 584 [1508.02294].
- [41] M. Wells, J.W. Pel, A. Glasse, G.S. Wright, G. Aitink-Kroes, R. Azzollini et al., *The Mid-Infrared Instrument for the James Webb Space Telescope, VI: The Medium Resolution Spectrometer, Publications of the Astronomical Society of the Pacific* **127** (2015) 646 [1508.03070].
- [42] <https://jwst-docs.stsci.edu/jwst-mid-infrared-instrument#gsc.tab=0>.
- [43] <https://archive.stsci.edu/>.
- [44] “Jwst background model.” <https://jwst-docs.stsci.edu/jwst-general-support/jwst-background-model>, year=2017, note = Accessed: 2023-08-07.
- [45] G. Cowan, K. Cranmer, E. Gross and O. Vitells, *Asymptotic formulae for likelihood-based tests of new physics*, *Eur. Phys. J. C* **71** (2011) 1554 [1007.1727].
- [46] B.M. Roach, S. Rossland, K.C.Y. Ng, K. Perez, J.F. Beacom, B.W. Grefenstette et al., *Long-exposure NuSTAR constraints on decaying dark matter in the Galactic halo*, *Phys. Rev. D* **107** (2023) 023009 [2207.04572].
- [47] CAST collaboration, *An Improved limit on the axion-photon coupling from the CAST experiment*, *JCAP* **04** (2007) 010 [hep-ex/0702006].
- [48] CAST collaboration, *New CAST Limit on the Axion-Photon Interaction*, *Nature Phys.* **13** (2017) 584 [1705.02290].
- [49] C. Severino and I. Lopes, *Asteroseismology: Looking for Axions in the Red Supergiant Star Alpha Ori*, *Astrophys. J.* **943** (2023) 95 [2212.01890].
- [50] C. O’Hare, “cajohare/axionlimits: Axionlimits.” <https://cajohare.github.io/AxionLimits/>, July, 2020. 10.5281/zenodo.3932430.
- [51] A. Caputo, C.A.J. O’Hare, A.J. Millar and E. Vitagliano, *Dark photon limits: a cookbook*, **2105.04565**.
- [52] J.F. Navarro, C.S. Frenk and S.D.M. White, *A Universal density profile from hierarchical clustering*, *Astrophys. J.* **490** (1997) 493 [astro-ph/9611107].
- [53] J. Einasto, *On the Construction of a Composite Model for the Galaxy and on the Determination of the System of Galactic Parameters*, *Trudy Astrofizicheskogo Instituta Alma-Ata* **5** (1965) 87.
- [54] A. Burkert, *The structure of dark matter halos in dwarf galaxies*, *The Astrophysical Journal* **447** (1995) .
- [55] D.J. Schlegel, D.P. Finkbeiner and M. Davis, *Maps of dust infrared emission for use in estimation of reddening and cosmic microwave background radiation foregrounds*, *The Astrophysical Journal* **500** (1998) 525–553.
- [56] G.M. Green, E. Schlafly, C. Zucker, J.S. Speagle and D. Finkbeiner, *A 3d dust map based on gaia, pan-starrs 1, and 2mass*, *The Astrophysical Journal* **887** (2019) 93.
- [57] J. Gao, A. Li and B.W. Jiang, *Modeling the infrared extinction toward the galactic center*, *Earth, Planets and Space* **65** (2013) 1127–1132.

## Appendix A: Polynomial Fit and Statistical Analysis

The astrophysical backgrounds include zodiacal light, detector thermal self-emission, stray light, and interstellar medium (ISM) background associated with the Galactic dust emission. For each mass  $m_a$ , I describe the photon emission from axions as a Gaussian centered on wavelength  $\lambda_a = 4\pi/m_a$  with variance  $\sigma^2 = \sigma_\lambda^2 + \sigma_0^2$ , where  $\sigma_\lambda^2$  is associated to the instrumental response and  $\sigma_0^2$  includes the Doppler shift, as described in Section II. The background is expected to be mostly smooth over the wavelength range covered by the axion line width. To avoid assuming a parametric form, I model the local background over a narrow range as a polynomial function:

$$p_n(\lambda) = \sum_{k=0}^n c_k (\lambda - \lambda_a)^k, \quad (\text{A1})$$

where the index  $k$  runs from 0 to the polynomial order  $n$ ,  $c_k$  are the polynomial coefficients and  $\lambda$  are the observed wavelengths in the spectrum. I fit this polynomial to the data which consists of a set of observed wavelength  $\lambda_i$ , their corresponding fluxes  $d_i$  and error on the fluxes  $\sigma_i$ , with the index  $i$  running over the data points within the narrow range centered on  $\lambda_a$ . I can determine the best-fitting coefficients via the goodness of fit,  $\chi^2$ , defined as

$$\chi^2 = \sum_i \left( \frac{p_n(\lambda_i) + \phi_a(\lambda_i) - d_i}{\sigma_i} \right)^2, \quad (\text{A2})$$

where  $\phi_a$  denotes the expected axion signal for a mass  $m_a$  and axion-photon coupling  $g_{a\gamma\gamma}$ , as described in Section 2. For convenience, let us define  $g_i = d_i - \phi_a(\lambda_i)$ . The best-fitting  $c_k$  are the ones that minimize the  $\chi^2$ , and I can solve for them by setting  $\partial\chi^2/\partial c_k = 0$  for all  $k$ . The resulting set of coefficients  $c_k$  can be written compactly as

$$\vec{c} = \mathbf{L}^{-1} \mathbf{P} \vec{g}, \quad (\text{A3})$$

where  $\vec{c}$  is the set of coefficients  $\{c_k\}$  and  $\vec{g}$  is the set of redefined fluxes  $\{g_i = d_i - \phi_a(\lambda_i)\}$ . The  $(n+1) \times (n+1)$  matrix  $\mathbf{L}$  has components given by

$$L_{kj} = \sum_i \frac{(\lambda_i - \lambda_a)^{k+j}}{\sigma_i^2}, \quad (\text{A4})$$

and the  $n \times h$  matrix  $\mathbf{P}$  reads

$$P_{ki} = \frac{(\lambda_i - \lambda_a)^k}{\sigma_i^2}, \quad (\text{A5})$$

where  $h$  is the number of data points in the narrow range where the fit is performed, while  $k$  and  $j$  are indices running from 0 to  $n$ .

The order of the polynomial used in this analysis is  $n = 4$ . Appendix B discusses the choice of the width of the narrow region, while Appendix C discusses the impact of the choice of the order  $n$  in the polynomial fit.

### Appendix B: Width of the region in the polynomial fit

The polynomial function described in the previous section is computed locally, over a narrow range of wavelengths. The width of this range is taken as the coherence length of the background fluctuations. The main challenge is that the background contains line features similar in width to the axion signal, and it is crucial for this analysis that the background subtraction does not spuriously remove line emission. Therefore, it is necessary to remove these line features before determining the coherence length of the background. The first step of this procedure requires identifying a line feature in the data to filter the signal out. This can be done by using something like a matched filter, that is by multiplying the data by the expected line shape

$$\int d\lambda \mathcal{F}(\lambda|\lambda_0) d(\lambda), \quad (\text{B1})$$

where  $d(\lambda)$  represents the data, the filter  $\mathcal{F}$  is the shape of the axion flux, determined by  $\left(\frac{df}{d\nu} * \mathcal{W}\right)$  and  $\lambda_0$  stands for the center of the line. I compensate the filter such that for a constant measured flux Eq. (B1) = 0. Therefore, I define the quantity

$$Q(\lambda_0) = \int d\lambda \mathcal{G}(\lambda|\lambda_0) d(\lambda), \quad (\text{B2})$$

where  $\mathcal{G} = \mathcal{F} - \mathcal{K}$ , and the function  $\mathcal{K}$  is a 1D tophat function centered on  $\lambda_0$  such that  $\int d\lambda \mathcal{F}(\lambda|\lambda_0) = \int d\lambda \mathcal{K}(\lambda|\lambda_0)$ . Therefore, if the observed flux  $d$  is constant,  $Q = 0$ . This way the function  $Q$  identifies lines and not the smooth background. The width of  $\mathcal{K}$  is given by  $10 \sigma$  ( $\pm 5\sigma$  centered on  $\lambda_0$ ), where  $\sigma$  is the root mean square of the assumed Gaussian profile of the DM line. Different choices for the width of  $\mathcal{K}$  ( $\pm 3\sigma$  and  $\pm 4\sigma$ ) lead to variations in the resulting bounds lower than 3%.

The second step of this procedure requires the identification of a threshold above which I label a feature as a line to be removed. The variance of the filtered spectrum is

$$\sigma_Q^2(\lambda_0) = \langle Q^2(\lambda_0) \rangle - \langle Q(\lambda_0) \rangle^2. \quad (\text{B3})$$

In the case of a pure background with no line features,  $\langle Q \rangle = 0$ . Therefore,  $\sigma_Q^2 = \langle Q^2(\lambda_0) \rangle$ .

From Eq. (B2), it follows

$$Q^2(\lambda_0) = \int d\lambda \int d\lambda' \mathcal{G}(\lambda|\lambda_0) d(\lambda) \mathcal{G}(\lambda'|\lambda_0) d(\lambda'), \quad (\text{B4})$$

thus

$$\langle Q^2 \rangle = \int d\lambda \int d\lambda' \mathcal{G}(\lambda|\lambda_0) \mathcal{G}(\lambda'|\lambda_0) \langle d(\lambda) d(\lambda') \rangle. \quad (\text{B5})$$

The noise is assumed to have diagonal covariance, therefore  $\langle d(\lambda)d(\lambda') \rangle$  is diagonal. Because the spectrum is observed in discrete pixels, I rewrite the integral as a sum:

$$\begin{aligned} \langle Q^2 \rangle &\approx \sum_{i,j} \mathcal{G}(\lambda_i|\lambda_0) \mathcal{G}(\lambda'_j|\lambda_0) \langle d(\lambda_i)d(\lambda'_j) \rangle \Delta\lambda_i \Delta\lambda_j \\ &= \sum_{i,j} \mathcal{G}(\lambda_i|\lambda_0) \mathcal{G}(\lambda'_j|\lambda_0) \sigma_i^2 \delta_{ij} \Delta\lambda_i \Delta\lambda_j \\ &= \sum_i \mathcal{G}^2(\lambda_i|\lambda_0) \sigma_i^2 \Delta\lambda_i^2, \end{aligned} \quad (\text{B6})$$

where  $\sigma_i$  is the error bar on the measured flux and  $\Delta\lambda$  is the pixel width.

I remove lines when  $Q(\lambda_0)$  differs from zero by more than  $\pm 2\sigma_Q$  (to remove both absorption and emission lines) and replace the removed fluxes by linearly interpolating between the edges of the excised region. I define  $\mathcal{D}$  as the new dataset with the lines removed. The autocorrelation function of  $\mathcal{D}$  is

$$\xi(\Delta\lambda) = \langle \mathcal{D}(\lambda) \mathcal{D}(\lambda + \Delta\lambda) \rangle - \langle \mathcal{D} \rangle^2, \quad (\text{B7})$$

where  $\langle \dots \rangle$  indicated the average over all wavelengths and observations. The variance of the new dataset is  $\sigma_{\mathcal{D}}^2 = \xi(0)$ . I define the coherence scale as the separation at which the correlation function  $\xi$  is half of the variance  $\sigma_{\mathcal{D}}^2$ . I find an average coherence scale that varies from  $0.17 \sim 0.25 \mu\text{m}$  (depending on  $\lambda_0$ ) for NIRSpec observations and  $0.32 \sim 1.21 \mu\text{m}$  for MIRI blank-sky fields. This is the scale I use for subtracting the local background when searching for an axion line and determining the limits on the axion-photon coupling  $g_{a\gamma\gamma}$ .

### Appendix C: Tests for Systematics

In this section, I estimate the impact of various systematics related to the background and axion modeling.

**Background uncertainty.** As described in Appendix A and B, the background emission is described by a polynomial fitted over a region of width given by the coherence length. This analysis assumes a polynomial of order 4. I assess the sensitivity of the result to the polynomial order by considering polynomials of order 3 and 5. The axion limits change by up to 7%.

**Dark matter density profile uncertainty.** The constraints derived above depend on the assumed D-factor  $\mathcal{D}$ , which is essentially the projected surface density of dark matter (DM) in each sightline. I estimated  $\mathcal{D}$  using the Navarro-Frenk-White (NFW) profile with halo parameters  $r_s = 24 \text{ kpc}$ ,  $\rho_s = 0.18 \text{ GeV/cm}^3$  [52]. To assess the impact of uncertainty in the assumed halo DM profile, I repeat the analysis for two alternative DM profiles: the Einasto profile with parameters  $r_s = 11 \text{ kpc}$ ,  $\rho_s = 0.43 \text{ GeV/cm}^3$  and  $\alpha = 0.16$  [53]; and the Burkert profile with parameters  $r_s = 12.67 \text{ kpc}$  and  $\rho_s = 0.712 \text{ GeV/cm}^3$  [54].

The analysis shows that, for the most part, the choice of profile has a minimal impact on the resulting constraints, with variations of less than 20%. However, in the mass range of 0.8–1.5 eV, where the Galactic Center’s DM density plays a crucial role in setting the limits, the constraints can change by up to 36% depending on the chosen profile.

**Sensitivity to individual targets** I use jackknife resampling to test whether the constraints are dominated by a small subset of the targets. I consider a few dark matter masses where the axion limits appear more oscillating (e.g.  $m_{\text{DM}} = 0.115 \text{ eV}$  and  $m_{\text{DM}} = 0.169 \text{ eV}$  for MIRI,  $m_{\text{DM}} = 1.034 \text{ eV}$  and  $m_{\text{DM}} = 1.113 \text{ eV}$  for NIRSpec). I compute the bounds by excluding one target at a time. I find that the distribution has a peak and a very narrow tail, which extends no further than 10% the mean value of the distribution. This suggests that the bounds is not dominated by a few targets.

**Astrophysical foregrounds and systematics in the galactic plane.** The Galactic plane is expected to suffer from the most astrophysical contamination of the DM signal from foregrounds and other systematics like absorption, including both broadband absorption (e.g., from dust extinction) and absorption from atomic and molecular lines. Dust extinction decreases sharply at longer wavelengths, and for the lines of sight considered in the analysis, broadband dust extinction is unimportant in NIRSpec and MIRI [55, 56]. The exceptions are near-infrared observations close to the Galactic Center [57].

Because these systematics should be most severe in the Galactic plane, I repeat my analysis after masking  $30^\circ$  above and below the Galactic Center. This reanalysis indicates that removing the targets on the Galactic plane has little effect on the resulting constraints, with variations remaining below 25%. However, in the mass range of 0.8–1.5 eV, where observations of the Galactic Center drive the limits, the constraints can shift by up to 64%, still far below the QCD axion DM band.



## Appendix D: Absorption lines

In the previous appendix, I considered the effects of broadband dust extinction. Another type of absorption to consider is line absorption due to molecular and atomic lines which can exist both inside and outside of the Galactic plane. To prevent the axion bounds from being affected by possible astrophysical absorption lines, I exclude the observations where an absorption line is present at  $\lambda_0 = 4\pi/m_{\text{DM}}$  with a significance greater than  $2\sigma_Q$ , where  $\sigma_Q$  is given by Eq. (B3). The first step requires the identification of an absorption line. I follow the same procedure of Appendix B up to Eq. (B6) to identify a line. In particular, the absorption lines correspond to emissions such that  $Q(\lambda_0)$  differs from zero by more than  $-2\sigma_Q$ . For every  $\lambda$ , I search for an absorption line in a specific observation and, if it presents, I do not utilize that observation to compute the bound for that specific value of  $\lambda_0$ .